

## Research



**Cite this article:** V V S Vara Prasad G, Dhar P, Samanta D. 2023 Triggering of electro-elastic anti-superhydrophobicity during non-Newtonian droplet collision. *Proc. R. Soc. A* **479**: 20220612.  
<https://doi.org/10.1098/rspa.2022.0612>

Received: 19 September 2022

Accepted: 6 July 2023

**Subject Areas:**

mechanical engineering, fluid mechanics

**Keywords:**

non-Newtonian fluids, droplets, electro-elastic effect, superhydrophobicity, electric Eotvos number, electric Weissenberg number

**Authors for correspondence:**

Purbarun Dhar

e-mail: [purbarun@mech.iitkgp.ac.in](mailto:purbarun@mech.iitkgp.ac.in)

Devranjan Samanta

e-mail: [devranjan.samanta@iitrpr.ac.in](mailto:devranjan.samanta@iitrpr.ac.in)

Electronic supplementary material is available online at <https://doi.org/10.6084/m9.figshare.c.6751624>.

# Triggering of electro-elastic anti-superhydrophobicity during non-Newtonian droplet collision

Gudlavalleti V V S Vara Prasad<sup>1</sup>, Purbarun Dhar<sup>2</sup> and Devranjan Samanta<sup>1</sup>

<sup>1</sup>Department of Mechanical Engineering, Indian Institute of Technology Ropar, Punjab 140001, India

<sup>2</sup>Hydrodynamics and Thermal Multiphysics Lab (HTML), Department of Mechanical Engineering, Indian Institute of Technology Kharagpur, West Bengal 721302, India

GVVSVP, 0000-0002-7960-6034; PD, 0000-0001-5473-2993; DS, 0000-0002-3406-1472

The present article discusses the electrohydrodynamics of impacting non-Newtonian dielectric droplets on superhydrophobic (SH) surfaces. The role of important parameters like electric Eotvos number ( $Eo_e$ ), Weber number ( $We$ ), dielectric particle concentration ( $TiO_2$ ) and polymer concentration ( $PEG-400$ ) were elucidated in this experimental study. Due to the interplay of non-Newtonian effects and electric field, we had observed the suppression of drop rebound on SH surfaces at much lower  $Eo_e$  compared to its Newtonian counterpart. It has been observed that with an increase in both polymer concentration or dielectric particle concentration, the suppression of drop rebounds was observed at lower  $Eo_e$ . In order to encapsulate the combined effects of electric field and non-Newtonian dynamics on drop rebound suppression, we have introduced the 'electro-elastic effect'. Contrary to the common observations of drop rebound on SH surfaces, this electro-elastic effect induces inhibition of drop rebound, thereby resulting in anti-superhydrophobicity. Subsequently, we also established a scaling relationship to show that the rebound suppression is observed as a manifestation of the onset of electro-elastic instability, when a proposed electric Weissenberg number ( $Wi_e$ ) exceeds unity. Finally, we demarcated the rebound and rebound suppression regimes of droplet dynamics through a detailed phase map.

# 1. Introduction

The impact hydrodynamics of liquid droplets, Newtonian fluids or otherwise, on different surfaces in the presence of external electric or magnetic fields [1] has great importance in many applications, such as inkjet printing [2], ferrohydrodynamic three-dimensional inkjet printing [3], magnetic drug targeting in microfluidic applications [4], spray painting, spray cooling [5], controlling the liquid metal droplet deposition during welding or soldering [6], electrohydrodynamic (EHD) droplet-on-demand inkjet printing [7], electro spraying [8,9], electrowetting [10] electrohydrodynamic jet (E-jet) [11] printing and so forth.

Several theoretical and experimental works have reported the EHDs of dielectric droplets under electric field in electrowetting and microfluidic applications. For instance, Nelson *et al.* [12] reviewed droplet actuation by electrowetting on dielectric (EWOD). They summarized the responsible forces which act on liquid droplets and their response in EWOD microfluidic devices. Torabinia *et al.* [13] proposed a new electromechanical model to predict the actuation of liquids in EWOD devices, and energy dissipation by contact line friction is treated in the form of a resistor, which explains contact angle hysteresis (CAH), line tension, etc. during EWOD. Wagoner *et al.* [14] theoretically studied the EHDs of lenticular drops and equatorial streaming. They showed that a lenticular drop's equatorial profile can be a wedge due to normal current condition within the droplet. Mousavi *et al.* [15] numerically studied the dynamics of droplet detachment from hydrophilic and hydrophobic surfaces under electric field through the Lattice Boltzmann method. Their findings highlighted the influence of several factors, including the Eotvos number ( $Eo$ ), capillary number ( $Ca$ ), Ohnesorge number ( $Oh$ ) and the dielectric constant on the deformation of droplets (oblate/prolate) with varying degrees of wettabilities. Pollack *et al.* [16] experimentally studied the actuation of microdroplets of aqueous electrolytes for integrated microfluidics based on electrowetting. They revealed that dependence of velocity on voltage is independent of droplet size and reported that using average velocities results in faster and more efficient droplet transport. Zeng *et al.* [17] investigated electrical controlled droplet-based laboratories on chip devices, working on the principles of electro-capillarity and dielectrophoresis. They conducted a study on the effects of EWODs and electrophoresis on droplet generation and manipulation. Their findings revealed that dielectrophoresis resulted in a reduction of contact angles and wetting contribution. Park *et al.* [18] described the electro-hydrodynamically induced fluid flow through fine micro-nozzles for jet pattern printing with sub-micron resolution. They demonstrated the superiority of e-jet printing over traditional inkjet printing by achieving high levels of printing resolution. They suggested that reducing the nozzle dimensions further would allow for printing at even smaller scales, down to the nanoscale. Deng *et al.* [19] revealed the role of electric charge in microdroplets impacting on conducting surfaces and reported sessile droplets with reduced contact angle and increased evaporation rates. Das *et al.* [20] numerically investigated the EHD interactions of a pair of leaky dielectric droplets in a uniform electric field and discussed the stability of such compound droplets. They revealed that pairs of droplets may coalesce or repel each other in the presence of electric field. Additionally, they found that the stability of a compound droplet and the relative motion between a pair of droplets depend primarily on the charge relaxation time constant of both the ambient medium and the outer shell of the compound droplet.

Besides, many researchers have experimentally elucidated the impact or dynamic EHDs of dielectric droplets. Sahoo *et al.* [21] experimentally investigated the impact EHDs of dielectric liquid droplets on both hydrophilic and superhydrophobic (SH) surfaces. They reported the influence of the electric Capillary number on the onset of droplet rebound suppression. Yun *et al.* [22] investigated and described the mechanism of droplet rebound suppression by inducing non-axisymmetric drop deformation and kinetic energy transfer between orthogonal coordinate axes. Tan *et al.* [23] revealed the control over drop impact on hydrophobic surfaces based on alternating current electrowetting-on-dielectric (AC EWOD). They studied the impact control mechanism of AC signal on droplets by analysing changes in spread diameter and height under varying frequencies and amplitudes. They found that applying AC electrowetting

on dielectric resulted in diameter oscillations during the retraction stage, which neutralized the kinetic energy and inhibited rebound. Wang *et al.* [24] experimentally focused on the electrohydrodynamic atomization in a stable cone jet with a middle viscous liquid with low conductivity. They reported that jet breakup with multi-jet, varicose and kink instabilities are noted with an increased fluid flow rate. Sung *et al.* [25] experimentally investigated the maximum spreading of electrically charged droplets on dielectric substrates. They proposed a model to predict the maximum spreading ratio for electrically charged droplets using liquid–gas and liquid–solid interfacial tensions. Mahmoudi *et al.* [26] experimentally revealed the effect of interfacial electric pressure on the spreading of a dielectric droplet and predicted the dynamics of film spreading owing to corona discharge through a simplified model. Yurkiv *et al.* [27] numerically simulated and modelled the drop impact on both polar and non-polar surfaces during EWOD.

Although earlier studies have focused on the influence of electric field on drop impact dynamics, the same for non-Newtonian droplets remains sparsely explored. Non-Newtonian droplets, especially elastic fluid or Boger fluids, have been shown to arrest the droplet rebound on SH surfaces [28]. This has excellent potential for the reduction of pesticide wastage and soil contamination during crop spraying. Various mechanisms such as extensional viscosity [29], normal stress [30] and stretching of polymer chains near the receding contact line [31] were attributed to the slowdown of retraction dynamics and subsequent drop rebound suppression. Further studies [32] showed that polymer concentrations and impact velocity are critical parameters to trigger the regime of rebound suppression. Based on the shear rate near the contact line during the onset of retraction, they showed that the local Weissenberg number ( $Wi$ ) exceeding 1 is an essential requirement for the elastic effects to dominate and lead to arrested rebound. Recently, Gudlavalleti *et al.* [1] studied the effect of magnetic field on post impact non-Newtonian ferrofluid droplets of SH surfaces and showed that droplet rebound suppression occurs earlier when in the presence of a magnetic field. With increasing magnetic particle concentration, the rebound suppression starts at lower magnetic Bond numbers ( $Bo_m = B^2 D_0 / \mu_0 \sigma_{lv}$ , defined as the ratio of magnetic force to surface tension force. Here,  $B$ ,  $D_0$ ,  $\mu_0$  and  $\sigma_{lv}$  denote magnetic flux density, pre-impact droplet diameter, magnetic permeability of free space and surface tension, respectively. The combined influence of non-Newtonian effects and magnetic field are together termed the magneto-elastic effect. Similar to the classical Weissenberg number ( $Wi = \lambda \dot{\gamma}$ ,  $\lambda$ : relaxation time and  $\dot{\gamma}$ : shear rate, defined as the ratio of elastic forces to viscous forces), a magnetic Weissenberg number ( $Wi_M = Wi + [Wi^{1/2} Bo_m^2]$ , defined in such that the ratio of magneto-elastic forces to visco-capillary forces)  $\geq 1$  was proposed as a threshold parameter to quantify the onset of droplet rebound suppression.

In the present article, we explore the combined effect of non-Newtonian effects and electric field on the droplet collision phenomena with SH surfaces. We have examined each aspect of impact dynamics of non-Newtonian dielectric fluid droplets, such as the role of impact spreading dynamics over external electric Eotvos numbers ( $Eo_e$ ) ranging from 0 to 12. Next, we have highlighted the role of fluid elasticity (polymer concentration), dielectric constant (nanoparticles concentration) and Weber number ( $We$ ) on droplet rebound and its suppression kinetics, if any. We have formulated a modified form of the classical Weissenberg number, termed the *electric Weissenberg number* ( $Wi_e$ ) to incorporate the influence of non-Newtonian effects and electric field as a threshold parameter to quantify the triggering of droplet rebound suppression on SH surfaces. Finally, we segregated both rebound and rebound suppression regimes as a function of polymer concentration, dielectric nanoparticle concentration, and  $We$  through a detailed regime map.

## 2. Material and methods

### (a) Non-Newtonian dielectric fluids

The non-Newtonian dielectric fluids considered in this study were colloidal solutions of titanium dioxide ( $TiO_2$ ) nanoparticles dispersed in a non-Newtonian base fluid, composed of different

polymer (PEG-400) concentrations in deionized (DI) water. First, different (%V/V) compositions of polyethylene glycol (PEG-400, Sigma Aldrich, India) were added to DI water and homogenized by stirring. Next, different (%W/W) compositions of titanium dioxide ( $\text{TiO}_2$ ) (Alfa Aesar, India, greater than 98.5% purity) nanoparticles were dispersed into the polymer solutions. Next, the colloidal polymeric solutions were subjected to mechanical stirring followed by ultrasonication for 2 h to ensure colloidal stability. Similar to an earlier study [33], the pendant drop method was used to measure the surface tension of the non-Newtonian dielectric fluid droplets. The physical properties of the different test fluids have been tabulated in table 1. We have adopted a nomenclature to distinguish the fluid samples: a non-Newtonian dielectric fluid containing 'x' % (%V/V) polymer with 'y' % (%W/W)  $\text{TiO}_2$  nanoparticles dispersion is denoted as Px-Ty. For example, the sample P20-T10 contains 20% V/V polymer in DI water, and with 10% W/W of  $\text{TiO}_2$  nanoparticles dispersed in it. The family of Newtonian dielectric fluid is denoted with P0-Ty.

## (b) Superhydrophobic surfaces

The SH surfaces were fabricated by commercial spray (Neverwet Ultra Ever dry, USA) by following reported protocol [34,35]. For the surface preparation, all glass slides were thoroughly cleaned with DI water and acetone and oven-dried carefully. Next, SH spray was used to create a uniform coated layer over the glass slides. We used a contact angle goniometer (Holmarc, India) to measure the static equilibrium contact angle, the advancing and receding contact angles of different dielectric fluids on these SH surfaces. Subsequently, we calculated the CAH by following reported protocol [1]. The static equilibrium contact angles of water droplets and non-Newtonian dielectric fluid droplets on the spray-coated SH surfaces were measured to be  $156 \pm 3^\circ$  and  $153 \pm 2^\circ$ , respectively. From four individual measurements, the average CAH was estimated to be approximately  $4^\circ$ – $6^\circ$ .

## (c) Experimental set-up

The experimental set-up is similar to our earlier study on droplet impact [21]. Figure 1 illustrates the schematic of the experimental set-up, in which two aluminium strips ( $50 \times 20 \times 2$  mm) with attached wires were used as electrodes to generate a direct electric field of up to a maximum of 8 kV. Throughout this study, an electrode gap of 15 mm was maintained. A regulated, high-voltage DC power supply unit (Ionics, India) is used to generate the high voltage between the two electrodes. A high-speed camera (Photron, UK) with a 105 mm macro lens (Nikon) was used to capture the images. All images were recorded at 4000 fps and at  $1024 \times 1024$  resolution. An LED array was used for backlight illumination. To alter impact  $We$ , a digitized droplet dispenser unit (Holmarc, India) equipped with a chromatographic syringe with a 22-gauge needle (U-TEK, India) was used to release the droplets from different heights. The droplets were allowed to impact on the SH surfaces such that it is equidistant from the two electrodes to ensure the impact was within a uniform electric field. All experiments were conducted at room temperature at approximately  $25^\circ\text{C}$ .

## (d) Governing non-dimensional numbers

The drop impact dynamics has been quantified using non-dimensional numbers. The maximum non-dimensional elliptical diameter ( $\xi_{\max}$ ) is defined as the ratio of major axis diameter ( $D_{\text{major}}$ ) to minor axis diameter ( $D_{\text{minor}}$ ) of elliptically spreading non-Newtonian dielectric fluid droplets. Weber number ( $We = \rho U^2 D_0 / \sigma_{\text{drop}}$ ) quantifies the ratio of inertia force to surface tension force and electric Eotvos number ( $Eo_e = \epsilon_0 \epsilon_r E^2 / \sigma_{\text{drop}}$ ) quantifies the ratio of electric force to surface tension force, where  $D_{\text{major}}$ ,  $D_{\text{minor}}$ ,  $\xi_{\max}$ ,  $\rho$ ,  $U$ ,  $D_0$ ,  $\epsilon_0$ ,  $\epsilon_r$ ,  $E$  and  $\sigma_{\text{drop}}$  are the major axis diameter of elliptically spreading liquid lamella (considered only the liquid portion lies within the liquid rim) of the droplet, the minor axis of elliptically spreading liquid lamella (refer to electronic supplementary material, S2 to view the asymmetric spreading dynamics), maximum

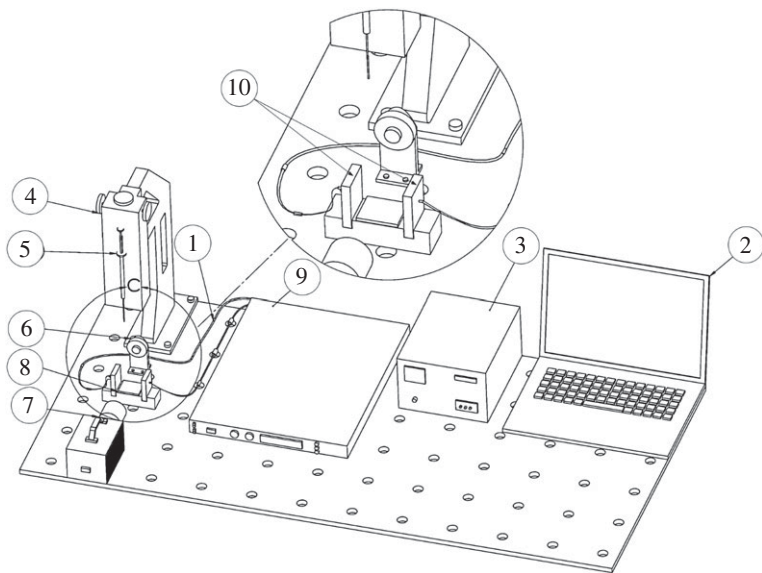


**Figure 1.** Schematic of the experimental set-up: (1) electrical wires, (2) computer for data acquisition and camera control, (3) DDM and backlight illumination controller, (4) droplet dispensing mechanism (DDM) unit, (5) microliter syringe, (6) LED array, (7) high-speed camera, (8) SH substrate, (9) high-voltage DC power supply unit and (10) electrode assembly.

**Table 1.** Physical properties of impacting non-Newtonian dielectric fluid droplets: density  $\rho$  ( $\text{kg m}^{-3}$ ), surface tension  $\sigma$  ( $\text{mN/m}$ ) and pre-impact droplet diameter  $D_0$  ( $\text{mm}$ ).

base fluid (PEG-400 concentration) (%V/V)	$\text{TiO}_2$ nanoparticles concentration (%W/W)	$\rho$	$\sigma$	$D_0$
0	0–10	997–1320.2	71–68.4	2.72–2.75
5	0–10	1003–1326	70.6–68.2	2.72–2.75
10	0–10	1009–1331	70.4–68.1	2.73–2.75
20	0–10	1018–1339	70.2–68.2	2.73–2.75

**Table 2.** Non-dimensional numbers of impacting non-Newtonian dielectric fluid droplets.

dimensionless parameter	expression	range
maximum non-dimensional elliptical diameter	$\xi_{\max} = D_{\text{major}}/D_{\text{minor}}$	0.98–1.24
Weber number ( $We$ )	$We = (\rho U^2 D_0)/\sigma_{\text{drop}}$	85–165
electric Eotvos number ( $Eo_e$ )	$Eo_e = (\epsilon_0 \epsilon_r E^2 D_0)/\sigma_{\text{drop}}$	0–12

non-dimensional elliptical diameter, density, impact velocity, pre-impact droplet diameter, the electrical permittivity of free space/vacuum ( $\epsilon_0 = 8.854 \times 10^{-12} \text{ F/m}$ ), the relative electrical permittivity of test fluids, electric field strength ( $\text{V/m}$ ) and surface tension of the fluids, respectively. The ranges of the non-dimensional numbers examined in this study are tabulated in table 2.



## (e) Electrorheology of the experimental fluids

Electrorheological (ER) characteristics of the various test fluids were performed to estimate the effective relaxation timescales of the fluid system. Akin to reports [36–41], all ER measurements were conducted using a rotational rheometer (Anton Paar, MCR-102). The rheometer was fit with an ER unit and operated in parallel plate mode. The temperature of the sample was controlled by an inbuilt Peltier unit and maintained at 25°C. First, we performed the shear-dependent flow curve rheology tests of the test fluids for various electric field strengths, ranging from 0 to 0.5333 kV mm<sup>-1</sup>. We observed that the degree of shear thinning increased with an increase in both polymer and nanoparticle concentrations in the absence of field (refer to electronic supplementary material, figures S1 and S2 for flow curve behaviour of test fluids).

Next, oscillatory shear ER (frequency sweep, constant amplitude of 1%) is performed. Based on a single mode of Maxwell fit (refer to electronic supplementary material, figure S3c in the supplemental document for the Maxwell fit), the single relaxation time ( $\tau_R$ ) is estimated from the storage modulus  $G'$  (electronic supplementary material, figure S3 in the supplemental document) and viscous modulus  $G''$  (electronic supplementary material, figure S3) by using the following relations:  $G'(\omega) = G_0 \omega^2 \tau_R^2 / (1 + \omega^2 \tau_R^2)$ ,  $G''(\omega) = G_0 \omega^2 \tau_R / (1 + \omega^2 \tau_R^2)$ . Based on the reported studies [42–45], the plateau modulus was estimated from the fixed value of  $G'$  at a higher operating angular frequency ( $\omega$ ), and relaxation time estimated from the following relation,  $\tau_R = 1/\omega_c$ , where  $\omega_c$  is the cross-over frequency as shown in the electronic supplementary material, figure S3c (electronic supplementary material, document). The relaxation time scales of the test fluids are tabulated in electronic supplementary material, tables S1–S3 (electronic supplementary material, document). From electronic supplementary material, table S1, it was observed that the relaxation time increases individually with an increase in electric field strength, polymer concentration and dielectric particle concentration provided the other two parameters were constant. As reported earlier [46,47], many researchers have revealed that in the presence of electric field,  $\text{TiO}_2$  nanoparticles behave like dipoles due to the polarization and form an anisotropic thin chain-like structure along the streamlines of the electric field. When a shear (during the spreading and retraction phases of the droplet) is applied, it destroys the chain structure [48] and consequently may affect the elastic nature of the polymer chains due to the increment in the relaxation time of the polymer chains over an external field.

## 3. Results and discussions

### (a) Spreading electrohydrodynamics of non-Newtonian droplets

We begin the discussions with the spreading dynamics of the non-Newtonian dielectric fluid droplets on SH surfaces for different  $E_{0e}$ . Figure 2a–d illustrates the influence of the  $E_{0e}$  on the spreading behaviour of non-Newtonian dielectric droplets by varying particle ( $\text{TiO}_2$ ) concentration at constant polymer (5% V/V) concentration and  $We \sim 65$ . In this work, we do not focus on the spreading electrohydrodynamics of Newtonian dielectric droplets, as has been discussed in detail in our previous work [21]. Figure 2a shows the spreading behaviour of pure polymer (P5-T0) droplets. During spreading, a liquid sheet and rim spread due to capillary and inertial forces. We analysed the shape of the sheet-rim (with a visible groove) during maximum spreading to measure non-uniform dynamics of electrically charged droplets. For each image, we attempted to fit the most appropriate circular or elliptical shape possible (blue-colour periphery). The droplet spreads with radial symmetry (throughout the study, we consider only the liquid lamella (refer to electronic supplementary material, §S2 to view the asymmetric spreading dynamics)) portion inside the liquid rim to describe the shape of spreading symmetry; see blue-colour peripheral boundary to identify the symmetry in figure 2). In the absence of electric field ( $E_{0e} \sim 0$ ), the P5-T0 droplets exhibit radial symmetry during spreading. The radius of the liquid lamella (refer to electronic supplementary material, §S2 to view the asymmetric spreading dynamics) during the maximum spreading stage becomes larger with an increase in

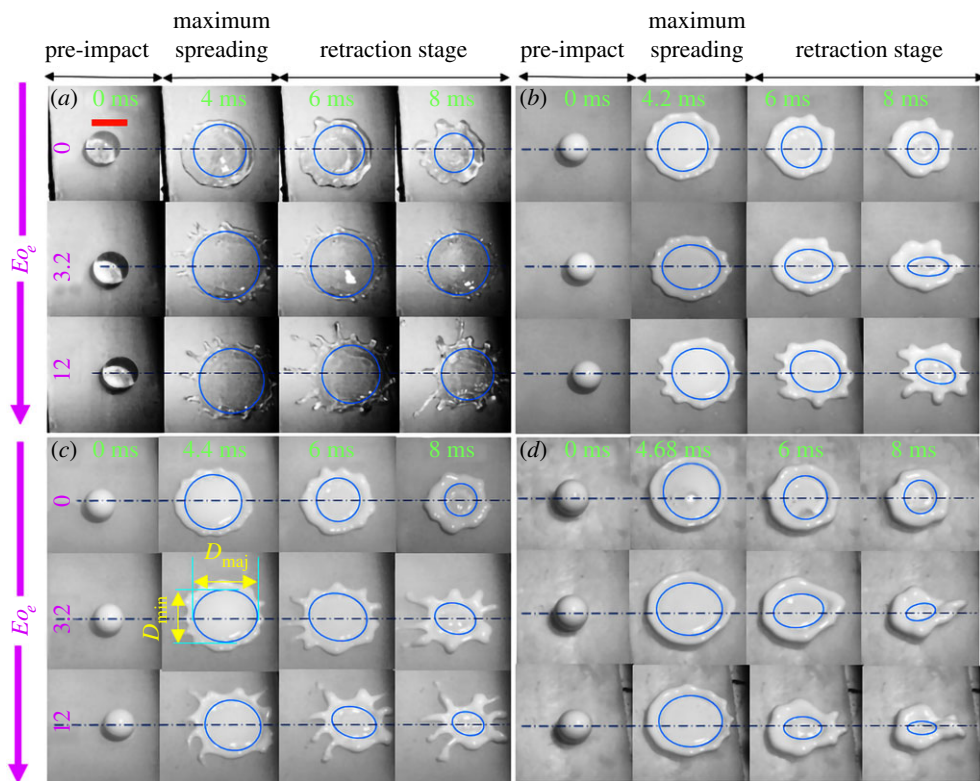


**Figure 2.** Temporal evolution of the spreading EHDs of non-Newtonian dielectric droplet for  $E_{0e}$  ranging from 0 to 12, at  $We \sim 65$  ( $U = 1.25$  m/s), for different fluids as (a) P5-T0 (b) P5-T2.5 (c) P5-T5 and (d) P5-T10. The scale bar represents 2.72 mm. Black dashes (— · —) represent the direction of electric field lines.

$E_{0e} \sim 3.2$  and 12. This signifies that the electrical body force on the polymer droplet is potent enough to augment the spreading, especially via the formation of radial spikes (refer to figure 2a, for  $E_{0e} = 12$ , at 6 ms to view the radial spikes).

When we increase the dielectric particle concentration at the same polymer concentration (sample P5-T2.5), the droplet still shows radial symmetry (first row of figure 2b) at  $E_{0e} \sim 0$ . But figure 2 (row 2 and 3) reveals that the droplet shape transits from radial symmetry to elliptical symmetry with increasing  $E_{0e} \sim 3.2$  to 12. The droplets start to elongate along the direction of the electric field during the spreading process, assuming elliptical shapes. The elliptical spreading enhances with an increase of  $E_{0e}$ .

For non-Newtonian dielectric droplets (refer to figure 2b,c), we also observed that the formation of spokes or filaments in the radial direction is more vigorous with an increase of  $E_{0e} \sim 12$ . Similarly, at higher dielectric particle concentration (at the same polymer concentration (P5-T5), the droplets still show the radial symmetry at  $E_{0e} = 0$ . But, the same droplets exhibit elliptically spreading liquid lamella (refer to second row and second column of figure 2c) even at moderate  $E_{0e} \sim 3.2$ . We infer that with an increase in  $E_{0e}$ , the onset of elliptical spreading is triggered with increase in the dielectric constant of the fluid (caused by increased dielectric particle concentration).

Analogous to previous studies [49], it is noteworthy to elucidate the recoiling behaviour of such non-Newtonian dielectric droplets during the retraction phase, against applied  $E_{0e}$ . As depicted in figure 2a–c, the droplet exhibits radial spokes through the liquid rim due to the fingering instability [49] at the liquid rim against the applied  $E_{0e}$ . Despite the induced corrugations or convolutions to the liquid rim during spreading and retraction stages, we believe that this may be due to the change in the dipole moment of the particles in the liquid sheet

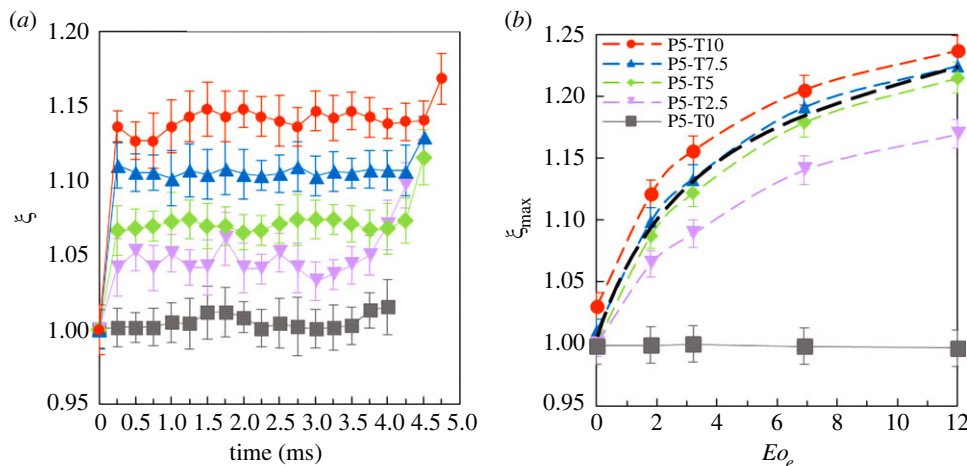


**Figure 3.** (a) Temporal evolutions of  $\xi$  from the instant of impact to the instant of attaining  $\xi_{\max}$  at  $We \sim 65$  and  $Eo_e = 3.2$ , (b) effect of dielectric particle concentration on  $\xi_{\max}$  for a fixed polymer concentration P5 at  $We \sim 65$  (i.e. at  $U = 1.25$  m/s). Black dashed line (— . —) in figure 3b represents the best polynomial fit.

in the presence of electric field. With increase of dielectric particle concentration, the fingering instability becomes more prominent. During early stages of spreading, the liquid rim displays the onset of fingers. These fingers may interact with each other to merge, or split based on the further expansion of the liquid rim [49]. But, at higher dielectric particle concentration (i.e. P5-T10), the transformation of spokes (fingers) into bulbous swelled liquid rim (refer figure 2d, 2nd row and 3rd column to view the fingering instability of liquid rim) is noted. This is due to the merging of fingers during both spreading and retraction stages against external  $Eo_e$ .

To quantify the asymmetric spreading dynamics, we have defined the ratio of the major axis to the minor axis as  $\xi_{\max} = (D_{\text{major}}/D_{\text{minor}})_{\max}$ . Figure 3a illustrates the temporal dynamics of  $\xi_{\max}$  for different fluids at  $Eo_e$  approximately 3.2. From figure 3a, it is observed that the droplet starts to elongate along the direction of the field within a few milliseconds of touching the substrate. In figure 3a,b,  $\xi_{\max} = 1$  implies radial symmetry for the whole range of  $Eo_e$  and occurs when the working fluid is devoid of any dielectric particles. For a fluid droplet with certain (non-zero) dielectric particle concentration, the  $\xi_{\max}$  increases monotonically from 1 with an increase in  $Eo_e$ . Also, for a fixed  $Eo_e$ ,  $\xi_{\max}$  increases with an increase in dielectric particle concentration. This is due to the increase in the EHD force in the droplets due to the increase of dielectric constant of the fluid with increased dielectric particle population.

Since pure non-Newtonian droplets do not exhibit elliptical spreading with an increase of  $Eo_e$  (figures 2 and 3a,b), it can be concluded that the elliptical spreading is induced by the effect of the electric field on the dielectric particles. The dielectric force acting on the droplet [20] is proportional to square of strength of electric field ( $E^2$ ) and the relative permittivity of the fluid,  $\epsilon_r$ . Hence with increase of  $Eo_e$  ( $\propto E^2$ ), the propensity to spread along the field direction increases. As noted from figure 3b, the  $\xi_{\max}$  of the non-Newtonian dielectric droplets over different  $Eo_e$  conforms to a third order polynomial with a measure of goodness of  $R^2 = 0.9981$  as  $\xi_{\max} = 1.0 + 0.0592(Eo_e) - 0.0065(Eo_e)^2 + 0.0003(Eo_e)^3$ .

## (b) Droplet rebound suppression (anti-superhydrophobicity) kinetics

### (i) Role of fluid elasticity (polymer concentration)

This section discusses the role of fluid elasticity (polymer concentration varied from P0 to P20) on the droplet rebound behaviour (for a fixed dielectric particle concentration T10) on SH surfaces for different  $Eo_e$  (figure 4) and at a fixed  $We \sim 85$ . The pure Newtonian droplets (P0, figure 4a)



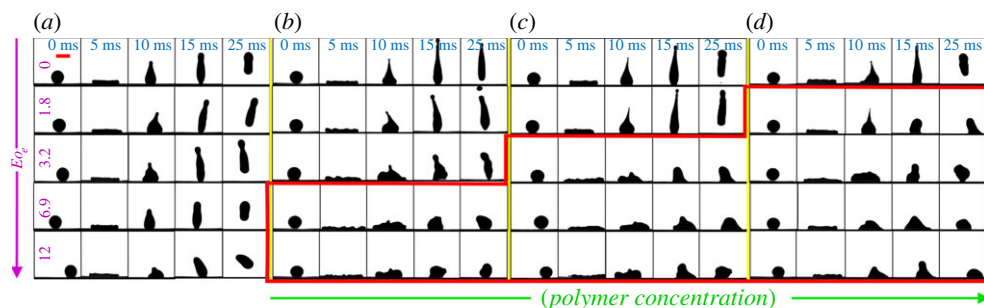


**Figure 4.** Effect of polymer concentration on non-Newtonian dielectric fluid droplet rebound for  $E_{0e}$  ranging from 0 to 12, at  $We \sim 85$  ( $U = 1.25$  m/s) for fluids as (a) P0-T10 (b) P5-T10 (c) P10-T10 and (d) P20-T10. The scale bar represents 2.72 mm. The red outline represents the cases where complete suppression of droplet rebound (anti-superhydrophobicity) is observed.

show no droplet rebound suppression for all  $E_{0e}$  investigated. Also, droplet rebound suppression was never noted for the non-Newtonian droplets in case of zero electric field. It was evident that with an increase in polymer concentration (fluid elasticity), the droplet rebound suppression (anti-superhydrophobicity) was observed at lower  $E_{0e}$  (red coloured circumscribed area in figure 4 for droplet rebound suppression).

For instance, rebound suppression was observed at  $E_{0e} \sim 6.9$  and 1.8, for P5-T10 and P20-T10, respectively. Hence, experiments reveal that (i) the coupled influence of fluid elasticity and EHD forces in the dielectric fluid leads to triggering of anti-superhydrophobicity effect and (ii) the rebound suppression is triggered at lower electric field strengths with increasing fluid elasticity. We believe, with increasing polymer concentrations, non-Newtonian effects such as the emergence of normal stresses slowing down the retraction dynamics gets augmented [32], resulting in lower threshold of  $E_{0e}$  to trigger arrest of droplet rebound.

## (ii) Role of fluid dielectric constant (particle concentration)

Figure 5 highlights the role of dielectric constant of the fluid (particle concentration ranging from T0 to T10) for a fixed polymer concentration (P20) for varying  $E_{0e}$  (0–12) on the droplet rebound behaviour. The non-Newtonian droplets with no dielectric particles could not inhibit droplet rebound for all  $E_{0e}$  (0–12). Droplet rebound suppression occurred at lower  $E_{0e}$  with the increase in dielectric particle concentration. Droplet rebound suppression was observed at  $E_{0e} \sim 6.9$  and 1.8 for P20-T5 and P20-T10 fluids (red coloured circumscribed area in figure 5), respectively. Therefore, from figure 5, it is evident that increase of dielectric particle concentration triggers rebound suppression at lower  $E_{0e}$ .

As discussed earlier [21], the dielectric force acting on the droplet is proportional to  $(E^2\epsilon)$ . This dielectric force is responsible for elliptic spreading of the droplets. In contrast with radial spreading, the capillary force responsible for retraction is hindered by the dielectric force in case of elliptic spreading. As a result, the retraction velocity reduces with increase in  $E^2\epsilon$ . This has been observed in our previous study [21], where rebound suppression on SH surface was observed with increase in electric field intensity for a Newtonian dielectric field. In the present scenario, we have noted that the onset of rebound suppression is largely reduced to lower values of  $E_{0e}$  when the non-Newtonian component is present in the fluids. Further, the threshold  $E_{0e}$  to trigger the rebound suppression is found to be decreasing with the increase in dielectric particle concentration.

This indicates the interactive role of non-Newtonian (elastic) effects with the EHD effects on rebound suppression kinetics. From electronic supplementary material, table S3 (electronic supplementary material), it is seen that for this set of fluids P20-T(0 to 10), the relaxation time increases with increase in the dielectric particle concentration. As we know, with increase

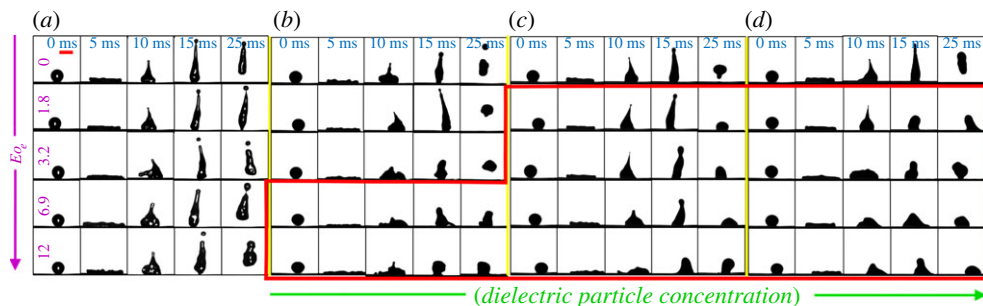


**Figure 5.** Effect of fluid dielectric constant (particle concentration) on non-Newtonian fluid droplet rebound suppression for  $E_{0e}$  ranging from 0 to 12, at  $We \sim 85$  ( $U = 1.25$  m/s) for fluids as (a) P20-T0, (b) P20-T5, (c) P20-T7.5 and (d) P20-T10. The scale bar represents 2.72 mm. The red outline represents the cases where complete suppression of droplet rebound (anti-superhydrophobicity) is observed.

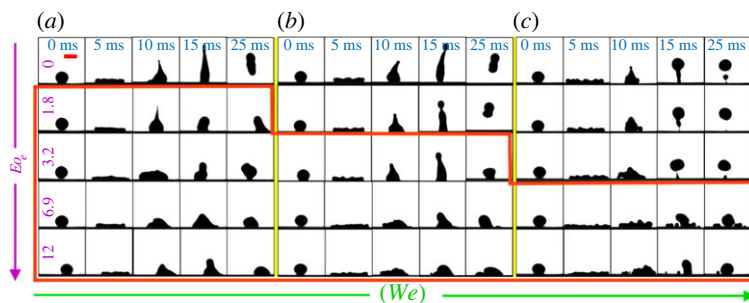


**Figure 6.** Effect of Weber number ( $We$ ) on non-Newtonian dielectric fluid droplet rebound suppression over different  $E_{0e}$  ranging from 0 to 12 for the case of P20-T10: (a)  $We \sim 85$  ( $U = 1.25$  m/s), (b)  $We \sim 120$  ( $U = 1.5$  m/s) and (c)  $We \sim 165$  ( $U = 1.75$  m/s). The scale bar represents 2.64 mm. The red outline represents the cases where complete suppression of droplet rebound (anti-superhydrophobicity) is observed.

in relaxation time, fluid elasticity is increased. With increase in elasticity, emergence of non-Newtonian features such as stretching of polymer chains [30], normal stress [29] slowing down the retraction process initiates, and subsequent rebound suppression occurs. So, at lower  $E_{0e}$ , for high dielectric particle concentration fluids, the elastic effects are already strong enough to hamper the receding dynamics. Therefore, the combined effect of polymers and increasing dielectric particle concentration leads to droplet rebound suppression at lower  $E_{0e}$ .

### (iii) Role of impact velocity (Weber number ( $We$ ))

Next, we highlight the role of Weber number (85–165) for a fixed fluid P20-T10 on the rebound dynamics, for varying  $E_{0e} \sim 0$  to 12, in figure 6. Rebound suppression was observed for higher  $E_{0e}$  with the increase in  $We$ . For instance, the rebound suppression was observed at  $E_{0e} \sim 1.8$  and 6.9 for  $We$  approximately 85 and 165, respectively. With increasing  $We$ , higher impact kinetic energy translates to availability of higher surface energy during the retraction phase and hence a higher propensity of rebounding. Thus, higher electric field intensity is required to reduce the retraction kinetic energy to inhibit the droplet rebound as  $We$  is increased. The observations signify that the onset of rebound is governed by the magnitude of shear during the retraction phase (the shear during spreading and retraction is dependent on the impact  $We$ ).

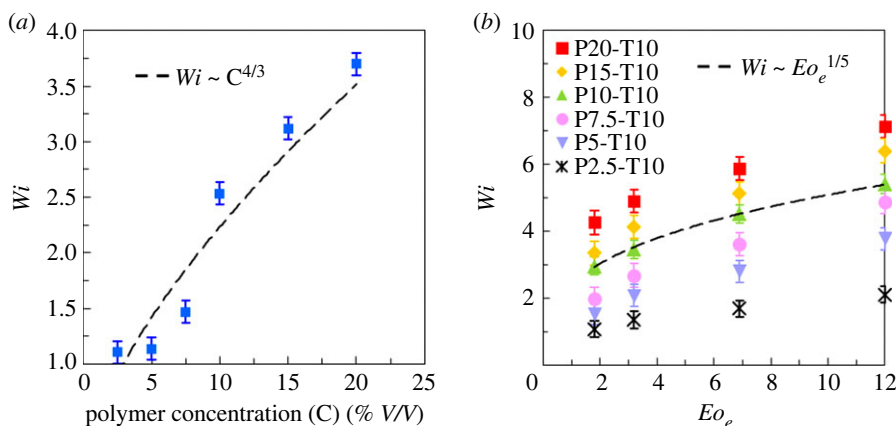
#### (iv) ‘Electro-elastic’ effect and role of electric Weissenberg number ( $Wi_e$ )

From the earlier §3b(i)–3b(iii), it is evident that the onset of rebound suppression occurs at lower  $Eo_e$  and this increases with an increase in fluid elasticity (polymer concentration) (figure 4) as well as fluid dielectric constant (particle concentration) (figure 5). Again, from figure 6 it was concluded that with an increase of  $We$ , initiation of droplet rebound suppression was observed at higher  $Eo_e$ . The droplet impact dynamics depends on the ER behaviour (dependent on polymer concentration, particle concentration and electric field strength) of the fluids and  $Eo_e$  (taking into account the electric field intensity and surface tension effects). We first quantify the Weissenberg number to estimate the role of fluid elasticity [50] during the droplet retraction phase. The  $Wi$  is calculated as the product of the relaxation time of the fluid and the average shear at the onset of retraction phase.

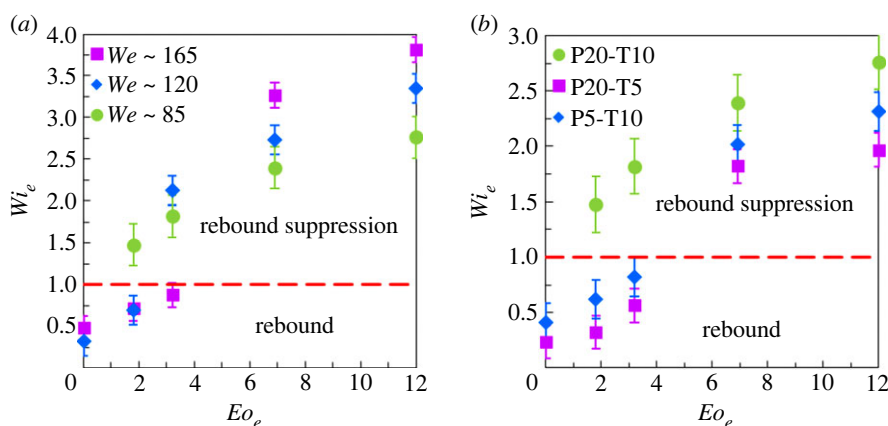
For the calculation of  $Wi$ , the relaxation time of the non-Newtonian solutions discussed earlier in §2e (electronic supplementary material, tables S1–S3 (in the electronic supplementary material, document)) was used. In addition, the shear rate was estimated at the moment of onset of retraction, based on protocols of previous studies on non-Newtonian droplets and flows [28,31]. Due to the generation of normal stress during retraction [32] and stretching of polymer chains near the receding contact line [51], the shear rate was calculated at the onset of retraction from image processing. To estimate the average shear rate during the onset of droplet retraction, we adopted the expression,  $\dot{\gamma} = du/dy = ((\Delta R/\Delta t)/\Delta y)$ , where  $\dot{\gamma}$ ,  $R$ ,  $y$  and  $t$  represent the retraction shear rate, liquid sheet radius during onset of retraction, liquid sheet height (thickness) during onset of retraction and time elapsed, respectively.

Figure 7a shows the influence of polymer concentration on  $Wi$  at a fixed  $We$ . Since the non-Newtonian effects hardly affect the spreading dynamics [28,31], the shear rate estimated during the onset of retraction (at fixed  $We$ ) will be of almost the same magnitudes for different polymer concentrations. Since the relaxation times usually increase with polymer concentration, it is evident that for a fixed  $We$  and consequently fixed shear rate,  $Wi$  will increase with concentration ( $C$ ), with an approximate scaling of  $Wi \sim C^{4/3}$  as obtained from figure 7a. Next, we tried to probe the influence of  $Eo_e$  on the  $Wi$  during the onset of retraction of non-Newtonian dielectric droplets for different concentrations (figure 7b). It can be observed that for a fixed  $We$ ,  $Eo_e$  and nanoparticle concentration, the  $Wi$  increased with the polymer concentration. Similarly, for a fixed  $We$  and any particular fluid, the  $Wi$  increased with the increase in  $Eo_e$  (since the fluids show different retraction dynamics in the presence of field). Since the  $Wi$  at a fixed  $We$  is dependent on relaxation time behaviour, the trends of figure 7b can be explained through the relaxation time trends presented in the electronic supplementary material, tables S1–S3 (in the supplemental document). From figure 7b,  $Wi$  was observed to scale in a best fit of power law as  $Wi \sim Eo_e^{1/5}$ .

The ‘electro-elastic effect’ is defined as the combined effect of both elastic effects of induced polymer chains (refer to figure 5) and EHDs of dielectric nanoparticles under external electric field (refer to figure 6) on rebound suppression of non-Newtonian dielectric droplets on SH surfaces. Since the pure elastic effects of polymer dynamics through the manifestation of  $Wi$  (refer to figure 7) and the pure EHDs of dielectric particles through  $Eo_e$  cannot provide a complete picture of the EHDs of non-Newtonian dielectric droplets, it is essential to provide the overall justification by joining both effects. In order to quantify the electro-elastic effect, we need to combine both elastic effects due to polymer dynamics and the EHD behaviour. With the aid of scaling analysis, we propose a new non-dimensional number, the *electric Weissenberg number*  $Wi_e = Wi + [1/2Wi^{2/3}Eo_e^{1/5}]$ . The  $Wi_e$  and the exponents of its constituents are defined in such a fashion that the onset of *electro-elastic* rebound suppression is demarcated by the regime  $Wi_e \geq 1$ . This is analogous to our earlier observed criteria of  $Wi \geq 1$  for rebound arrest in the case of pure non-Newtonian droplets [32] and magnetic Weissenberg number ( $Wi_M$ )  $\geq 1$  in the case of non-Newtonian ferrofluid droplet rebound suppression [1] by magneto-elastic phenomenon. The values of  $Wi_e$  for P20-T10 droplets with different impact  $We$  against varied  $Eo_e$  have been illustrated in figure 8a. We emphasize that the threshold electric Weissenberg number ( $Wi_e > 1$ ) criterion can segregate the regimes of rebound and rebound suppression (inhibition) with respect



**Figure 7.** Electro-elasto-hydrodynamics of the non-Newtonian dielectric fluid droplet during the onset of retraction at  $We \sim 85$ : (a) role of fluid elasticity (polymer concentration) on Weissenberg number ( $Wi$ ) for P2.5 to P20 with same dielectric particle concentration (T10) (b) map of  $Eo_e$  with  $Wi$  for different fluids, showing a best fit of power law scaling.



**Figure 8.** Regime map of droplet impact outcomes with proposed electric Weissenberg number ( $We_e$ ) against  $Eo_e$ : (a) map of  $We_e$  for different  $We$  for P20-T10 fluid and (b) map of  $We_e$  for different fluids at  $We \sim 85$ .

to both impact  $We$  and applied  $Eo_e$  and has been highlighted in figure 8a,b. Hence, based on this proposed non-dimensional number, the electro-elastic paradigm and its manifestation of anti-superhydrophobic behaviour by the non-Newtonian dielectric droplets can be quantified and mapped.

Figures 6 and 8a summarize the influence of impact  $We$  on non-Newtonian dielectric droplet rebound suppression. For a fixed working fluid P20-T10, it is evident that for lower  $We$  approximately 85, rebound suppression was observed for the whole range of  $Eo_e$  measured in our study. The rebound suppression was observed at higher  $Eo_e$  at higher  $We$  only. The low electric field strength was reasonably sufficient to inhibit the dielectric droplet rebound against low retraction shear rates by overcoming stored kinetic energy. But, when the same droplet impacts with a higher  $We$ , the droplet needs higher electric field strengths to overcome the higher retraction shear rates. Thus, from figure 8a, we confer that the non-Newtonian dielectric droplet of the case P20-T10, the droplet impacts relatively with higher  $We$  (i.e. approximately 165) needs higher electric field strength (i.e. higher  $Eo_e$ ) to suppress the droplet rebound.

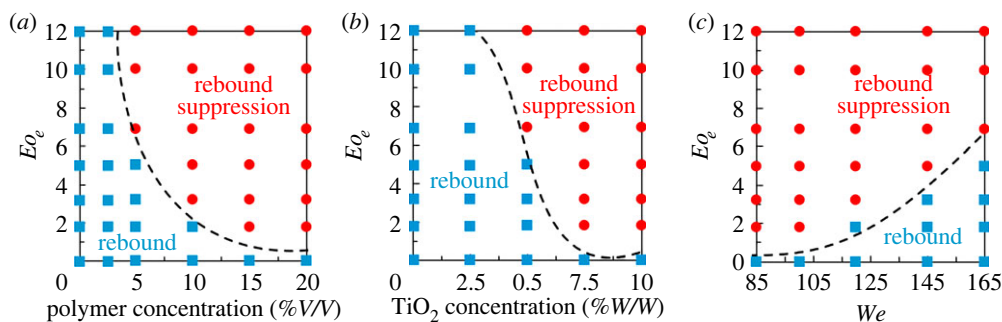


**Figure 9.** Demarcation of both rebound and no rebound (rebound suppression) regimes: (a) effect of  $E_{0e}$  over polymer concentration at  $We \sim 85$ , (b) effect of  $E_{0e}$  over dielectric nanoparticles concentration at  $We \sim 85$  and (c) effect of  $E_{0e}$  over  $We$  for a particular fluid P20-T10.

From figures 4 and 8b, it is clear that the probability of rebound suppression increases with the increase in polymer concentration (P5 and P20) for a fixed dielectric particle concentration (T10). This is obvious as the relaxation time increases with polymer concentration and subsequently  $Wi$ . Consequently, the chance of  $Wi_e > 1$  is higher with increased polymer concentration for a fixed dielectric particle concentration (refer to electronic supplementary material, table S2 in the electronic supplementary material). Similarly, in reference to electronic supplementary material, table S3, relaxation time increased with an increase in dielectric particle concentration for a fixed polymer concentration. So, at a fixed polymer concentration of P20, the higher dielectric particle concentration fluid P20-T10 tends to inhibit droplet rebound compared to P20-T5.

#### (v) Regime map of rebound and rebound suppression in drop impact dynamics

Finally, we have prepared the phase maps highlighting the demarcation zone of drop rebound and rebound suppression as a function of  $E_{0e}$  versus polymer concentration, dielectric particle concentration and  $We$  in figure 9a–c, respectively; from figure 9a, it is evident that the probability of rebound suppression at lower  $E_{0e}$  increases with an increase in polymer concentration. Again, for a fixed polymer concentration, the probability of rebound suppression increases with an increase in  $E_{0e}$ . Figure 9b shows similar trends to figure 9a. The onset of rebound suppression was observed at lower  $E_{0e}$  with an increase in  $TiO_2$  concentration. At a particular  $E_{0e}$  and  $We$ , the rebound suppression phenomena trigger an increase in polymer concentration. The droplet with low polymer concentration needs higher electric  $E_{0e}$  to get rebound suppression (refer to figure 9a to view the rebound arrestment of the droplet).

On the other hand, the dielectric particle concentration of a droplet of the same polymer concentration at a fixed  $E_{0e}$  and  $We$  triggers rebound suppression phenomena. The droplet with high dielectric particle concentration requires higher  $E_{0e}$ . We also investigated a particular case of non-Newtonian dielectric fluid droplets of P20-T10, the influence of  $We$  on droplet rebound suppression against external  $E_{0e}$  and infer that droplet has a higher propensity to exhibit rebound suppression relatively at lower  $We$ . Since droplet impacts with lower  $We$ , contains develop lower shear rates during retraction. Hence, the lower electric field strength is quite sufficient to retard the drop retraction by overcoming the stored kinetic energy. But, in the case of the droplet with higher  $We$  it needs more electric field strength to retard the drop retraction at higher shear rates due to the larger amount of stored kinetic energy of the droplet (refer to figure 9c to view the segregation of both rebound and no-rebound behaviours of the droplet).



## 4. Conclusion

In this study, we report an experimental investigation of the EHDs of non-Newtonian dielectric droplets on SH surfaces in the presence of an external DC electric field. We used stable colloidal solutions of dielectric particles ( $TiO_2$ ) dispersed in polymeric solutions as the non-Newtonian dielectric fluids. This study encompasses a range of  $We \sim 85$ – $165$  and  $Eo_e \sim 0$ – $12$ . We observed that the non-dimensional maximum elliptical spreading ( $\xi_{max}$ ) increases with dielectric particle concentration at a fixed polymer concentration and  $We$  against external electric  $Eo_e$ . Through the experimental investigations, we examined the effects of polymer concentration, dielectric particle concentration,  $We$  and  $Eo_e$  on the impact EHDs of non-Newtonian dielectric droplets. We also emphasized the role of polymer concentration, dielectric particle concentration and  $We$  on non-Newtonian droplet rebound suppression kinetics over external DC electric field in terms of  $Eo_e$ . With the thorough experimental examination, increasing polymer and dielectric particle concentration, the drop rebound suppression triggers with an increase of  $Eo_e$ . But decreasing  $We$  for a particular polymer and dielectric particle concentration triggers the onset of rebound. The findings of this research could assist future researchers in developing new strategies to minimize ink wastage caused by droplet rebound suppression from external fields in alternative printing techniques such as EHD inkjet printing, magnetohydrodynamic (MHD) inkjet printing, droplet and ferrofluidic manipulation, and so on.

**Ethics.** This work did not require ethical approval from a human subject or animal welfare committee.

**Data accessibility.** We have shared relevant raw material of rheological measurements as electronic supplementary material.

All data are presented and provided within this paper and the electronic supplementary material document.

The data are provided in the electronic supplementary material [52].

**Authors' contributions.** GVVSP: investigation and writing—original draft; P.D.: conceptualization, methodology, supervision and writing—review and editing; D.S.: conceptualization, investigation, methodology, project administration, resources, supervision and writing—review and editing.

All authors gave final approval for publication and agreed to be held accountable for the work performed therein.

**Conflict of interest declaration.** The authors do not have any conflicts of interest with any individuals or agencies with respect to the current research work.

**Funding.** GVVSP would like to thank the Ministry of Education, Govt. of India, for the doctoral scholarship. D.S. would like to thank IIT Ropar for partially funding the work (vide grant no. 9-246/2016/IITRPR/144). P.D. thanks IIT Kharagpur (vide grant ISIRD SFI) and Science and Engineering Research Board (SERB) (vide grant no. SRG/2020/000004) for partially funding the work.

**Acknowledgements.** The authors would like to thank Dr. Prabhat K. Agnihotri, Department of Mechanical Engineering, IIT Ropar, for access to the high-voltage power supply unit.

## References

1. Vara Prasad GVVS, Dhar P, Samanta D. 2021 Magneto-elastic effect in non-Newtonian ferrofluid droplets impacting superhydrophobic surfaces. *Langmuir* **37**, 9673–9682. (doi:10.1021/acs.langmuir.1c00885)
2. Yarin AL. 2006 Drop impact dynamics: splashing, spreading, receding, bouncing.... *Annu. Rev. Fluid Mech* **38**, 159–192. (doi:10.1146/annurev.fluid.38.050304.092144)
3. Karampelas IH, Vader S, Vader Z, Sukhotskiy V, Verma A, Garg G, Tong M, Furlani E. 2017 Drop-on-demand 3D metal printing. *Adv. Mater. TechConnect Briefs* **4**, 153–155.
4. Gijs MAM, Lacharme F, Lehmann U. 2010 Microfluidic applications of magnetic particles for biological analysis and catalysis. *Chem. Rev.* **110**, 1518–1563. (doi:10.1021/cr9001929)
5. Visser CW, Pohl R, Sun C, Römer GW, Huis B, Veld T, Lohse D. 2015 Toward 3D printing of pure metals by laser-induced forward transfer. *Adv. Mater* **27**, 4087–4092. (doi:10.1002/adma.201501058)
6. Wu H, Chang Y, Lu L, Bai J. 2017 Review on magnetically controlled arc welding process. *Int. J. Adv. Manuf. Technol.* **91**, 4263–4273. (doi:10.1007/s00170-017-0068-9)
7. Tunel M. 2019 Developing the High-Resolution Electrohydrodynamic (EHD) 3D Jet Printing System for Thermoplastic Materials. PhD thesis. Philadelphia, PA: Drexel University.

8. Gañán-Calvo AM, Dávila J, Barrero A. 1997 Current and droplet size in the electrospraying of liquids. Scaling laws. *J. Aerosol Sci* **28**, 249–275. (doi:10.1016/S0021-8502(96)00433-8)
9. Cloupeau M, Prunet-Foch B. 1994 Electrohydrodynamic spraying functioning modes: a critical review. *J. Aerosol. Sci.* **25**, 1021–1036. (doi:10.1016/0021-8502(94)90199-6)
10. Mugele F, Baret JC. 2005 Electrowetting: from basics to applications. *J. Phys. Condens. Matter.* **17**, R705. (doi:10.1088/0953-8984/17/28/R01)
11. Mishra S, Barton KL, Alleyne AG, Ferreira PM, Rogers JA. 2010 High-speed and drop-on-demand printing with a pulsed electrohydrodynamic jet. *J. Micromech. Microeng.* **20**, 095026. (doi:10.1088/0960-1317/20/9/095026)
12. Nelson WC, Kim CJC. 2012 Droplet actuation by electrowetting-on-dielectric (EWOD): a review. *J. Adhes. Sci. Technol* **26**, 1747–1771. (doi:10.1163/156856111X599562)
13. Torabinia M, Farzbod A, Moon H. 2018 Electromechanical model to predict the movability of liquids in an electrowetting-on-dielectric microfluidic device. *J. Appl. Phys.* **123**, 154902. (doi:10.1063/1.5014045)
14. Wagoner BW, Vlahovska PM, Harris MT, Basaran OA. 2021 Electrohydrodynamics of lenticular drops and equatorial streaming. *J. Fluid Mech.* **925**, 1–23. (doi:10.1017/jfm.2021.651)
15. Mousavi SE, Moshfegh A, Afrouzi HH, Javadzadegan A, Toghraie D. 2020 Simulation of droplet detachment from hydrophobic and hydrophilic solid surfaces under the electric field using Lattice Boltzmann Method (LBM). *J. Mol. Liq.* **313**, 113528. (doi:10.1016/j.molliq.2020.113528)
16. Pollack MG, Shenderov AD, Fair RB. 2002 Electrowetting-based actuation of droplets for integrated microfluidics. *Lab. Chip* **2**, 96–101. (doi:10.1039/b110474h)
17. Zeng J, Korsmeyer T. 2004 Principles of droplet electrohydrodynamics for lab-on-a-chip. *Lab. Chip* **4**, 265–277. (doi:10.1039/b403082f)
18. Park JU *et al.* 2007 High-resolution electrohydrodynamic jet printing. *Nat. Mater.* **6**, 782–789. (doi:10.1038/nmat1974)
19. Deng W, Gomez A. 2010 The role of electric charge in microdroplets impacting on conducting surfaces. *Phys. Fluids* **22**, 1–4. (doi:10.1063/1.3431739)
20. Das SK, Dalal A, Tomar G. 2021 Electrohydrodynamic-induced interactions between droplets. *J. Fluid Mech.* **915**, 1–27. (doi:10.1017/jfm.2021.120)
21. Sahoo N, Samanta D, Dhar P. 2021 Electrohydrodynamics of dielectric droplet collision with variant wettability surfaces. *Phys. Fluids* **33**, 112005. (doi:10.1063/5.0065609)
22. Yun S, Hong J, Kang KH. 2013 Suppressing drop rebound by electrically driven shape distortion. *Phys. Rev. E Stat. Nonlinear Soft Matter. Phys* **87**, 1–5. (doi:10.1103/PhysRevE.87.033010)
23. Tan J, Wang H, Sun M, Tian P, Wang Y, Wang K, Jiang D. 2021 Regulating droplet impact on a solid hydrophobic surface through alternating current electrowetting-on-dielectric. *Phys. Fluids* **33**, 042101. (doi:10.1063/5.0044823)
24. Wang Q, Wang Z, Yang S, Li B, Xu H, Yu K, Wang J. 2021 Experimental study on electrohydrodynamic atomization (EHDA) in stable cone-jet with middle viscous and low conductive liquid. *Exp. Therm. Fluid Sci.* **121**, 110260. (doi:10.1016/j.expthermflusci.2020.110260)
25. Ryu SU, Lee SY. 2009 Maximum spreading of electrically charged droplets impacting on dielectric substrates. *Int. J. Multiph. Flow* **35**, 1–7. (doi:10.1016/j.ijmultiphaseflow.2008.09.003)
26. Mahmoudi SR, Adamiak K, Castle GSP. 2011 Spreading of a dielectric droplet through an interfacial electric pressure. *Proc. R. Soc. A* **467**, 3257–3271. (doi:10.1098/rspa.2011.0220)
27. Yurkiv V, Yarin AL, Mashayek F. 2018 Modeling of droplet impact onto polarized and nonpolarized dielectric surfaces. *Langmuir* **34**, 10 169–10 180. (doi:10.1021/acs.langmuir.8b01443)
28. Bergeron V. 2003 Designing intelligent fluids for controlling spray applications. *Comptes Rendus Phys.* **4**, 211–219. (doi:10.1016/S1631-0705(03)00043-4)
29. Smith MI, Bertola V. 2010 Effect of polymer additives on the wetting of impacting droplets. *Phys. Rev. Lett.* **104**, 1–4. (doi:10.1103/PhysRevLett.104.154502)
30. German G, Bertola V. 2009 Impact of shear-thinning and yield-stress drops on solid substrates. *J. Phys. Condens. Matter* **21**, 375111. (doi:10.1088/0953-8984/21/37/375111)
31. An SM, Lee SY. 2012 Observation of the spreading and receding behavior of a shear-thinning liquid drop impacting on dry solid surfaces. *Exp. Therm. Fluid Sci.* **37**, 37–45. (doi:10.1016/j.expthermflusci.2011.09.018)

32. Dhar P, Mishra SR, Samanta D. 2019 Onset of rebound suppression in non-Newtonian droplets post-impact on superhydrophobic surfaces. *Phys. Rev. Fluids* **4**, 103303. (doi:10.1103/PhysRevFluids.4.103303)
33. Vara Prasad GVVS, Dhar P, Samanta D. 2022 Postponement of dynamic Leidenfrost phenomenon during droplet impact of surfactant solutions. *Int. J. Heat Mass Transf.* **189**, 122675. (doi:10.1016/j.ijheatmasstransfer.2022.122675)
34. Sahoo N, Khurana G, Samanta D, Dhar P. 2021 Collisional ferrohydrodynamics of magnetic fluid droplets on superhydrophobic surfaces. *Phys. Fluids* **33**, 012012. (doi:10.1063/5.0032610)
35. Sahoo N, Dhar P, Samanta D. 2022 Colloids and surfaces â physicochemical and engineering aspects vertical magnetic field aided droplet-impact-magnetohydrodynamics of ferrofluids. *Colloids Surfaces A Physicochem. Eng. Asp.* **633**, 127872. (doi:10.1016/j.colsurfa.2021.127872)
36. Yapici K, Cakmak NK, Ilhan N, Uludag Y. 2014 Rheological characterization of polyethylene glycol based TiO<sub>2</sub> nanofluids. *Korea-Australia Rheol. J.* **26**, 355–363. (doi:10.1007/s13367-014-0041-1)
37. Tseng WJ, Lin K. 2003 Rheology and colloidal structure of aqueous TiO<sub>2</sub> nanoparticle suspensions. *Mater. Sci. Eng. A* **355**, 186–192. (doi:10.1016/S0921-5093(03)00063-7)
38. Harzallah OA, Dupuis D. 2003 Rheological properties of suspensions of TiO<sub>2</sub> particles in polymer solutions. *Rheol. Acta* **42**, 10–19. (doi:10.1007/s00397-002-0250-2)
39. Chen H. 2007 Rheological behaviour of ethylene glycol based titania nanofluids. *Chem. Phys. Lett.* **444**, 333–337. (doi:10.1016/j.cplett.2007.07.046)
40. Dhar P, Saini V, Chattopadhyay A, Samanta D. 2021 Electro-viscoelasticity of agarose based electrorheological fluids. *Phys. Fluids* **33**, 013101. (doi:10.1063/5.0037105)
41. Yan SR, Toghraie D, Abdulkareem LA, Alizadeh A, Barnoon P, Afrand M. 2020 The rheological behavior of MWCNTs–ZnO/water–ethylene glycol hybrid non-Newtonian nanofluid by using of an experimental investigation. *J. Mater. Res. Technol.* **9**, 8401–8406. (doi:10.1016/j.jmrt.2020.05.018)
42. Zhang W, Gao Z, Zhu H, Zhang Q. 2021 Mixed micellization of cationic/anionic amino acid surfactantsâ synergistic effect of sodium lauroyl glutamate and alkyl tri-methyl ammonium chloride of sodium lauroyl glutamate and alkyl tri-methyl ammonium chloride. *J. Dispers. Sci. Technol.* **0**, 1–13. (doi:10.1080/01932691.2021.1929289)
43. Tee HT, Zipp R, Koynov K, Tremel W, Wurm FR. 2020 Poly (methyl ethylene phosphate) hydrogelsâ degradable and cell-repellent alternatives to PEG-hydrogels. *Eur. Polym. J* **141**, 110075. (doi:10.1016/j.eurpolymj.2020.110075)
44. Matter S, Haward SJ, Ober TJ, Oliveira SN, Alves A, McKinley GH. 2012 Extensional rheology and elastic instabilities of a wormlike micellar solution in a microfluidic cross-slot device. **8**, 536–555. (doi:10.1039/c1sm06494k)
45. Haward SJ. 2019 Flow of wormlike micellar solutions around microfluidic cylinders with high aspect ratio and low blockage ratio. *Soft Matter*. **15**, 1927–1941. (doi:10.1039/c8sm02099j)
46. Cheng Y, Zhao Z, Wang H, Hua L, Sun A, Wang J, Li Z, Guo J, Xu G. 2021 Strong electrorheological performance of smart fluids based on TiO<sub>2</sub> particles at relatively low electric field. *Front. Mater.* **8**, 1–10. (doi:10.3389/fmats.2021.764455)
47. Zhao XP, Zhao Q, Gao XM. 2003 Optical activity of electrorheological fluids under external electric field. *J. Appl. Phys.* **93**, 4309–4314. (doi:10.1063/1.1559435)
48. Lenglov A, Pavlinek V, Sha P, Quadrat O, Kitano T, Stejskal J. 2003 Influence of particle concentration on the electrorheological efficiency of polyaniline suspensions. *Eur. Polym. J.* **39**, 641–645. (doi:10.1016/S0014-3057(02)00281-1)
49. Lee M, Chang YS, Kim HY. 2010 Drop impact on microwetting patterned surfaces. *Phys. Fluids* **22**, 1–7. (doi:10.1063/1.3460353)
50. Samanta D, Dubief Y, Holzner M, Schfer C, Morozov AN, Wagner C, Hof B. 2013 Elasto-inertial turbulence. *Proc. Natl Acad. Sci. USA* **110**, 10557–10562. (doi:10.1073/pnas.1219666110)
51. Moon JH, Kim DY, Lee SH. 2014 Spreading and receding characteristics of a non-Newtonian droplet impinging on a heated surface. *Exp. Therm. Fluid Sci.* **57**, 94–101. (doi:10.1016/j.expthermflusci.2014.04.003)
52. V V S Vara Prasad G, Dhar P, Samanta D. 2023 Triggering of electro-elastic anti-superhydrophobicity during non-Newtonian droplet collision. Figshare. (doi:10.6084/m9.figshare.c.6751624)